Research Square

Preprints are preliminary reports that have not undergone peer review.
They should not be considered conclusive, used to inform clinical practice,
or referenced by the media as validated information.

Intensifying phosphorus limitation accelerates the global decline of the CO_2 fertilization effect

Jing Peng

peng.j275@mail.sysu.edu.cn

Sun_Yat_Sen University

Zhuo Zhang

Chengjin Chu

Shenzhen Campus of Sun Yat-sen University https://orcid.org/0000-0002-0606-449X

Wenjie Dong

Sun Yat-sen University https://orcid.org/0000-0002-9635-6292

Li Dan

Institute of Atmospheric Physics https://orcid.org/0000-0001-8759-9412

Yaping Chen

Sun Yat-sen University https://orcid.org/0000-0003-1372-8861

Article

Keywords:

Posted Date: September 28th, 2026

DOI: https://doi.org/10.21203/rs.3.rs-10982549/v1

License: This work is licensed under a Creative Commons Attribution 4.0 International License.
Read Full License

Additional Declarations: There is **NO** Competing Interest.

Abstract

Terrestrial ecosystems absorb about one-third of anthropogenic CO_2 emissions, largely sustained by the CO_2 fertilization effect (CFE). Yet the global CFE is declining, and it remains untested whether this decline is driven primarily by water stress or by intensifying phosphorus limitation. Here we integrate multiple remote-sensing gross primary production (GPP) products, CABLE land-surface simulations with coupled carbon–nitrogen–phosphorus cycling, and structural equation modelling (SEM) to quantify these links. We find that regions of intensifying phosphorus limitation experienced the fastest CFE decline during 1982–2015 (β: −2.28% per 100 ppm yr^{-1}, versus − 2.24% globally), alongside faster reductions in interannual GPP increments—despite milder, not harsher, hydroclimatic stress. This climate–response mismatch indicates that climatic deterioration alone cannot explain the regional decline. Instead, SEM showed the leaf N:P–GPP relationship shifted from insignificant globally to significantly negative in these regions, where its contribution to GPP variance (10.6%) approached that of vapour pressure deficit (11.2%). Rising carbon-to-phosphorus ratios across plant, litter, and soil pools further indicate intensifying stoichiometric imbalance. These results demonstrate that phosphorus limitation rivals climate in driving CFE decline, and that neglecting dynamic phosphorus cycling likely causes Earth system models to overestimate future carbon sink potential.

Introduction

Terrestrial ecosystems absorb about one-third of anthropogenic CO_2 emissions and therefore play a central role in moderating climate change[1]. A substantial part of this land carbon uptake is associated with the CO_2 fertilization effect (CFE), whereby rising atmospheric CO_2 enhances plant photosynthesis and terrestrial carbon assimilation[2]. Elevated CO_2 can increase photosynthetic carbon uptake by stimulating carboxylation [3], improve water-use efficiency through reduced transpiration [4,5], and amplify canopy-scale responses through increases in leaf area index (LAI). Accordingly, CFE has been widely recognized as an important driver of global greening and land carbon sink growth [6,7]. Understanding how CFE varies across space and time is therefore critical for projecting the persistence of the terrestrial carbon sink and its capacity to buffer future climate change.

Although CFE has long been considered a major contributor to land carbon sink enhancement, evidence from remote sensing and eddy-covariance observations suggests that the global CFE has declined since the 1980s. This weakening implies that the terrestrial carbon sink may be approaching saturation [8], with potential consequences for faster atmospheric CO_2 accumulation and stronger climate warming [9]. Importantly, the decline is spatially heterogeneous: stronger reductions have been reported in northern high latitudes, parts of Africa, South America, and Europe, whereas other regions show weaker changes or relative stability [3]. These spatial variations imply that global trends can conceal critical regional dynamics.

Water stress has been widely invoked as one of the main mechanisms reducing CFE. Increases in vapor pressure deficit (VPD) can partially offset the fertilization effect by constraining stomatal conductance

[10,11], and the water-saving benefits of elevated CO_2 have already shown saturation or weakening in some regions [12]. A recent study further showed that, since 2001, photosynthesis in drylands has been increasingly dominated by water stress, with strong suppression of CFE, whereas humid regions show little comparable offset [13]. These findings indicate that water limitation explains part of the observed CFE decline. However, the continued decline of CFE in relatively wet regions suggests that additional mechanisms remain insufficiently accounted for.

In fact, CFE emerges from the joint regulation of water supply and nutrient availability [14–17]. Both nitrogen (N) and phosphorus (P) limitations are known to weaken vegetation responses to elevated CO_2[18,19]. Recent evidence suggests that phosphorus limitation may now impose stronger constraints on global photosynthesis than nitrogen limitation, especially in tropical and some high-latitude ecosystems [20]. While the global land area under phosphorus limitation is expanding at a remarkable rate of approximately 7.4×10^5 km² yr^{-1} [21], it remains untested whether this intensification systematically corresponds to a faster decline in CFE. Quantitative attribution is still lacking to determine whether CFE decline in these regions is primarily driven by water stress or intensifying phosphorus constraints. Ultimately, global-scale conclusions may mask dominant mechanistic differences within key regions, thereby complicating projections of future terrestrial carbon sink sustainability.

Here we test the hypothesis that intensifying phosphorus limitation accelerates CFE decline and contributes to its spatial heterogeneity at the global scale. If this mechanism is important, then regions of intensifying phosphorus limitation should exhibit a faster CFE decline than the global average and than other regions, together with stronger stoichiometric constraints on productivity, even in the absence of harsher climatic stress. To test this, we combined long-term remote-sensing observations, simulations from the CABLE land surface model with coupled carbon–nitrogen–phosphorus (C–N–P) cycling, and structural equation modelling. Specifically, we: (1) quantified the spatiotemporal dynamics of CFE using NIRvGPP over 1982–2015; (2) identified regions of intensifying phosphorus limitation from CABLE simulations and examined their spatial correspondence with, and climatic background of, CFE decline; and (3) compared the regulatory pathways of GPP between the globe and these regions to evaluate whether nutrient stoichiometric constraints strengthen under intensifying phosphorus limitation.

Results

2.1. Faster β decline in regions of intensifying phosphorus limitation

To quantify vegetation productivity responses to rising CO_2, we estimated β at the pixel level from NIRvGPP after excluding grid cells with substantial land-cover change. The CO_2 fertilization response weakened significantly across the globe, and this decline was fastest in regions of intensifying phosphorus limitation. During 1982–2015, β declined at − 2.28 ± [0.35] % per 100 ppm yr^{-1} in regions of intensifying phosphorus limitation, faster than the global rate of − 2.24 ± [0.38] % per 100 ppm yr^{-1} and

than the rate in other regions (− 2.22 ± [0.39] % per 100 ppm yr^{-1}; all $p < 0.01$; Fig. 1c). This three-tiered gradient (− 2.28 > − 2.24 > − 2.22) indicates that intensifying phosphorus limitation was associated with the most rapid weakening of the CO_2 fertilization effect.

The sub-period comparison confirmed this ordering. The median β in regions of intensifying phosphorus limitation dropped from 28.89% per 100 ppm during 1982–1996 to 10.97% per 100 ppm during 2001–2015, alongside the global decline from 28.57% to 11.53% and that in other regions from 28.37% to 11.79% (Fig. 1d).

Spatially, the decline was widespread and geographically coherent. Within regions of intensifying phosphorus limitation, 76.03% of grid cells exhibited declining β and 50.78% showed statistically significant declines (Table S1). The strongest declines were concentrated in the tropical low latitudes and northern high latitudes, with only isolated grid cells showing local increases (Fig. 1a); zonal averages revealed a broadly coherent latitudinal pattern, interrupted only by a localized recovery near 30°N (Fig. 1b).

This pattern was robust across three independent GPP products. Based on rEC-LUEGPP, β declined at − 1.20 ± [0.34] globally versus − 1.30 ± [0.29] in regions of intensifying phosphorus limitation (both $p < 0.01$; Fig. S3c); based on VODCA2GPP, the corresponding rates were − 2.12 ± [0.24] versus − 2.23 ± [0.25] % per 100 ppm yr^{-1} (both $p < 0.01$; Fig. S4c). All products located the strongest declines in the tropical low latitudes and northern high latitudes (Figs. S3a, S4a).

Critically, the faster β decline in regions of intensifying phosphorus limitation did not coincide with harsher climatic stress. These regions did not experience more severe hydroclimatic conditions than the global mean: baseline VPD was lower than the global average, and although VPD increased significantly (0.04 hPa $decade^{-1}$; $p < 0.05$; Fig. S7c), this was only about one-third of the global mean; baseline SM was higher than the global average, and its decline (0.003 $m^3\ m^{-3}\ decade^{-1}$; $p < 0.05$; Fig. S7f) was comparable to the global trend. Warming and precipitation trends were both smaller than the global average (TMP: 0.15°C $decade^{-1}$; PRE: 0.47 mm $decade^{-1}$; Figs. S7a, b), and incoming shortwave radiation even increased faster than globally (Fig. S7e). Because these regions declined fastest despite milder, not harsher, climatic stress, the faster β decline cannot be attributed to climatic deterioration, implying that an intensifying nutrient — specifically phosphorus — constraint is the more parsimonious driver.

2.2. Vegetation-type-specific differences in β decline

The weakening of the CFE was widespread but markedly heterogeneous across vegetation functional types. β declined in all nine classes, yet its magnitude differed substantially. In four of the nine classes(ENF MF OS and WET),β declined faster within regions of intensifying phosphorus limitation than in their global averages, revealing strong functional-type heterogeneity. Mixed forest (MF) exhibited the largest decline: β decreased at − 4.64% per 100 ppm yr^{-1} globally and at − 4.92% per 100 ppm yr^{-1} in regions of intensifying phosphorus limitation — the steepest of any vegetation type (Fig. 2d). By contrast,

evergreen broadleaf forest (EBF) declined by only − 0.46% per 100 ppm yr^{-1} in both domains (Fig. 2b). This nearly tenfold difference underscores a pronounced functional-type divergence.

Two converging lines of evidence — relative sensitivity (β) and absolute productivity gain — identify MF as the most vulnerable type and EBF as the most resilient. In regions of intensifying phosphorus limitation, the absolute GPP response (change in GPP per 100-ppm increase; g C m^{-2} yr^{-1} per 100 ppm) of MF fell steeply from 486 to 99, whereas that of EBF declined more modestly, from 457 to 278 (Fig. S5). EBF retained a high baseline absolute response, which buffers its relative sensitivity and explains why its β remained nearly unchanged; MF, in contrast, lost the bulk of its productivity gain.

The disproportionate influence of MF is further amplified by its relative enrichment within regions of intensifying phosphorus limitation. MF occupies 6.35% of the total area of these regions (Tp/Ap), compared with 3.92% of global land area (Tg/Ag); the MF area situated within these regions accounts for 2.16% of global land area (Tp/Ag; Fig. 2d). MF therefore combines one of the strongest β declines with relative enrichment in phosphorus-limited regions.

Consistent with the whole-domain analysis, the faster β decline in MF cannot be explained by stronger water stress. VPD in MF increased at 0.06 hPa $decade^{-1}$ ($p < 0.05$; Fig. S8c), slightly below the global average of 0.07, while SM declined at 0.003 m^3 m^{-3} $decade^{-1}$ ($p < 0.05$; Fig. S8e), smaller than the global mean of 0.004. Thus, MF in these regions did not experience stronger water stress, reinforcing an intensifying phosphorus constraint as the explanation.

2.3. Faster decline in interannual GPP increments in regions of intensifying phosphorus limitation

To test whether CFE decline had propagated into productivity dynamics, we examined ΔGPP. Globally, ΔGPP declined during 1982–2015, and this decline was faster in regions of intensifying phosphorus limitation. Based on NIRvGPP, the global ΔGPP trend was − 0.53 g C m^{-2} yr^{-2}, versus − 0.61 in regions of intensifying phosphorus limitation (Fig. 3b).

Other products supported this. Based on rEC-LUEGPP, ΔGPP declined at − 0.31 (global) versus − 0.37 g C m^{-2} yr^{-2} (regions of intensifying phosphorus limitation; both $p < 0.05$; Fig. 3b). Based on VODCA2GPP, the global trend was negative but not significant, whereas ΔGPP declined significantly in regions of intensifying phosphorus limitation (− 0.32 g C m^{-2} yr^{-2}; $p < 0.05$; Fig. 3b).

Spatially, declining ΔGPP was widespread across regions of intensifying phosphorus limitation (Fig. 3a): the northern high latitudes and much of Africa were dominated by negative trends, with localized increases in central South America and parts of southern China. This distribution broadly matched the β decline pattern (Fig. 1a), indicating that weakening CO_2 sensitivity was accompanied by a synchronous slowdown in realized productivity growth.

Globally, all vegetation types except EBF showed significant ΔGPP declines ($p < 0.05$; Fig. 3c); within regions of intensifying phosphorus limitation, every type declined, with MF the steepest (− 1.50 versus −

1.35 g C m^{-2} yr^{-2} globally). MF thus emerges as the most vulnerable type in both the sensitivity (β) and realized-increment (ΔGPP) dimensions. Overall, regions of intensifying phosphorus limitation experienced both a faster β decline and a faster reduction in interannual GPP increments, indicating that weakening CFE has propagated into slower productivity growth, most acutely in MF.

2.4. Stronger stoichiometric constraints on GPP in regions of intensifying phosphorus limitation

To resolve the mechanisms underlying CFE decline, we constructed SEMs integrating climatic drivers, nutrient status, and vegetation traits globally and within regions of intensifying phosphorus limitation (Fig. 4). CO_2 remained the primary driver of GPP in both domains, and its direct effect was marginally stronger where phosphorus limitation intensified: the standardized CO_2→GPP path was 0.27 (95% CI: 0.19–0.33; $p < 0.05$; contribution 42.4%) globally and 0.33 (95% CI: 0.21–0.43; $p < 0.05$; 42.6%) in regions of intensifying phosphorus limitation (Fig. S6). Thus, the CFE decline did not arise from a loss of the direct CO_2–GPP coupling, but from countervailing constraints acting alongside it.

The decisive difference lay in the stoichiometric constraint on GPP, which shifted from negligible to significant. At the global scale, the leaf N:P–GPP relationship was indistinguishable from zero (β = −0.01; 95% CI: −0.10 to 0.06; $p > 0.05$), whereas in regions of intensifying phosphorus limitation it became significantly negative (β = −0.11; 95% CI: −0.24 to − 0.06; $p < 0.05$). This qualitative transition raised the relative contribution of leaf N:P to GPP to 10.6%, approaching that of VPD (11.2%; Fig. S6). Consistently, elevated CO_2 was associated with rising leaf N:P (path coefficients 0.12 globally, 95% CI: 0.05–0.20; and 0.17 in regions of intensifying phosphorus limitation, 95% CI: 0.11–0.27; both $p < 0.05$), while phosphorus deposition retained a weak negative effect on leaf N:P in both domains and the positive effect of nitrogen deposition became non-significant under intensifying phosphorus limitation.

Independent evidence from carbon–nutrient stoichiometry corroborated an intensifying phosphorus constraint (Fig. 5). Across soil, plant, and litter pools, C:P ratios increased more steeply in regions of intensifying phosphorus limitation than globally during 1982–2015, most pronounced in the woody (WOD) and root (ROT) plant pools, the slow soil pool (SLW), and the structural and coarse/woody litter pools (STR, COA; Fig. 5d–f). C:N ratios also rose, but the contrast was systematically sharper for C:P than for C:N (Fig. 5a–c versus 5d–f), indicating that carbon accumulation increasingly outpaced phosphorus relative to nitrogen.

In parallel, the relative importance of water stress receded as that of stoichiometry rose. VPD remained the strongest negative driver of GPP globally (direct effect − 0.18; 95% CI: −0.23 to − 0.12; $p < 0.05$; contribution 19.2%), but its direct effect weakened to − 0.12 (95% CI: −0.22 to − 0.03; $p < 0.05$) and its contribution fell to 11.2% in regions of intensifying phosphorus limitation, converging with that of leaf N:P. The positive residual covariance between LAI and WUE was also stronger in these regions (r = 0.25; 95% CI: 0.15–0.36) than globally (r = 0.14; 95% CI: 0.09–0.20; both $p < 0.05$). Overall, although the direct CO_2–GPP coupling persisted, the emergence of a significant leaf N:P–GPP constraint — corroborated by

steepening C:P trajectories — imposed a distinct stoichiometric brake on the productivity gains from rising CO_2, offering a nutrient-based mechanism for the faster CFE decline in these regions.

Discussion

Our combined satellite- and model-based analyses show that terrestrial CFE declined globally during 1982–2015 and that this decline was faster in regions of intensifying phosphorus limitation than globally or in other regions (Fig. 1c). Because CFE is a key mechanism sustaining land carbon uptake, future terrestrial carbon sink capacity may be overestimated where phosphorus constraints are increasing. Previous global studies emphasized increasing VPD as a major constraint on photosynthesis and CFE [22]. Our results extend this framework by showing that the CFE decline cannot be interpreted solely through water stress, but also requires consideration of regionally intensifying phosphorus limitation and the associated strengthening of nutrient stoichiometric imbalance. In regions of intensifying phosphorus limitation, the suppressive effect of leaf N:P imbalance on GPP became much stronger, likely reflecting increasing relative phosphorus deficiency. This is consistent with regional observations of increasing N:P under phosphorus stress [23] and with FACE experiments and meta-analyses showing reduced CO_2 responses under phosphorus limitation [24,25].

Regions of intensifying phosphorus limitation concentrated mainly in tropical low latitudes and northern high latitudes, although the mechanisms likely differ. In tropical low latitudes, phosphorus is commonly the dominant limiting nutrient [26]: long-term bedrock weathering depletes phosphorus while high rainfall promotes leaching [27,28], so long-term responses to elevated CO_2 are more likely constrained by phosphorus supply. Northern high-latitude ecosystems have traditionally been considered nitrogen limited, but our results, consistent with prior work, suggest relative phosphorus constraints may be increasing [29], possibly associated with rising nitrogen deposition and warming that raise phosphorus demand [30]; because phosphorus inputs depend largely on weathering, supply may not match rising demand [31]. Thus, intensifying phosphorus limitation can emerge through different mechanisms across climate zones while ultimately weakening sustained productivity responses to elevated CO_2 [32].

Response magnitude varied among vegetation types. MF showed the strongest β decline, likely related to its concentration in northern high latitudes where intensifying phosphorus limitation is widespread; MF is therefore more frequently exposed to increasing relative phosphorus deficiency. Because high-latitude forest productivity is sensitive to both canopy structure and leaf-level physiology, stronger phosphorus limitation may simultaneously constrain structural expansion and photosynthetic capacity, amplifying the β decline. EBF showed the weakest decline [33], possibly because tropical canopies and LAI are already high, and because species in chronically phosphorus-poor environments may possess stronger adaptive strategies — enhanced phosphorus acquisition and recycling, efficient internal allocation, and higher photosynthetic phosphorus-use efficiency [34,35]. Exogenous phosphorus from fire-derived deposition in parts of the Amazon may also locally alleviate limitation [36]. Declines in β were generally stronger at high than low latitudes, consistent with the MF–EBF contrast and prior work

[3]. This is particularly important in boreal and northern forests, critical for carbon sink growth [37], because strong MF declines imply greater uncertainty in future carbon sink stability.

At a mechanistic level, water stress alone is insufficient to explain the faster CFE decline in regions of intensifying phosphorus limitation, which occurred despite these regions not showing stronger water stress than the global mean (Fig. S7). Under global change, elevated CO_2 can still promote carbon uptake through enhanced photosynthesis, improved water-use efficiency, and reduced photorespiration [38], but this is increasingly offset by multiple constraints [39]. While rising VPD is widely regarded as weakening CFE by inducing stomatal closure [40], in regions of intensifying phosphorus limitation stoichiometric imbalance imposed a much stronger constraint on GPP, with an effect size approaching that of VPD. Because these regions declined fastest without stronger water stress, stoichiometric imbalance is likely a major regional constraint. Understanding CFE decline therefore requires a transition from a water-centric to a coupled water–nutrient framework [41].

The stoichiometric imbalance was characterized primarily by increasing relative phosphorus deficiency (Fig. 5). During 1982–2015, C:N changes were relatively small whereas C:P increased much more strongly, driving a persistent rise in N:P — consistent with faster declines in phosphorus than nitrogen concentrations [21]. Relative phosphorus deficiency is expected to constrain carbon assimilation first at the photosynthetic level, because phosphorus is required for ATP production, electron transport, and RuBP regeneration [42,43]. The strongest C:P increase occurred in woody organs (WOD), with smaller changes in leaves (LEF), suggesting plants prioritize leaf phosphorus homeostasis by diluting phosphorus in nonphotosynthetic tissues [21]. Elevated tissue C:P is transferred to soils via litter; structural litter (STR) showed a pronounced C:P increase, implying increasingly phosphorus-poor returns that may slow microbial decomposition and nutrient turnover [44,45]. Rising soil C:P suggests carbon accumulation increasingly outpaced phosphorus replenishment. Together, rising plant phosphorus demand, phosphorus-poor litter, and reduced soil phosphorus resupply may form a reinforcing feedback that strengthens ecosystem-scale N:P imbalance and further weakens productivity responses to elevated CO_2.

Several uncertainties should be acknowledged. First, the identification of regions of intensifying phosphorus limitation relies primarily on CABLE. Although CABLE is one of the few models explicitly representing coupled C–N–P cycling [46,47], its representation of long-term plant and microbial adaptation under low phosphorus remains limited [48], which may affect the spatial identification. Multi-model comparisons, nutrient-addition experiments, and long-term observations would help test these patterns. Second, β estimates may be influenced by disturbances not explicitly included, such as fire [49]; combining disturbance data with causal-inference approaches could improve attribution. Third, SEM results are sensitive to variable selection and path specification and should be interpreted as mechanistic evidence rather than proof of causality. Overall, the evidence supports a robust association between intensifying phosphorus limitation and faster CFE decline, but exact mechanisms require further testing.

Overall, our study suggests that intensifying phosphorus limitation may fundamentally weaken the capacity of terrestrial ecosystems to respond to rising CO_2 by inducing nutrient stoichiometric imbalances. Explaining and predicting CFE decline requires going beyond a water-stress-only framework to explicitly incorporate dynamic phosphorus limitation and its stoichiometric consequences. As climate change and nitrogen deposition intensify relative phosphorus scarcity, the extent of regions experiencing intensifying phosphorus limitation may expand [50,51], offsetting a larger fraction of CFE-related carbon sink gains [52–56]. If Earth system models do not adequately represent dynamic phosphorus cycling and its coupling with carbon and nitrogen, they may systematically overestimate future terrestrial carbon sink potential [58,59].

Conclusions

Using long-term remote sensing, CABLE simulations with coupled C–N–P cycling, and structural equation modelling, we assessed how intensifying phosphorus limitation affects the terrestrial CO_2 fertilization effect (CFE). We show that terrestrial CFE declined globally during 1982–2015, and that this decline was fastest in regions of intensifying phosphorus limitation (− 2.28% per 100 ppm yr^{-1}), exceeding the global average (− 2.24% per 100 ppm yr^{-1}) and other regions (− 2.22% per 100 ppm yr^{-1}; Fig. 1c). These regions also showed a faster reduction in interannual GPP increments, indicating a concurrent slowdown in productivity gains. This faster decline occurred despite these regions not experiencing harsher climatic stress, and thus cannot be explained by climatic deterioration alone. Instead, the negative relationship between leaf N:P and GPP strengthened markedly — shifting from non-significant globally to significant in regions of intensifying phosphorus limitation — with an explanatory contribution approaching that of VPD. This indicates that increasing relative phosphorus deficiency and the resulting stoichiometric imbalance are likely key constraints on sustained ecosystem responses to elevated CO_2. Concurrent increases in C:P and N:P across plants, litter, and soils suggest these constraints may be reinforced through ecosystem feedbacks.

Overall, explaining and predicting CFE decline requires moving beyond a water-stress-only framework to explicitly incorporate dynamic phosphorus limitation and its stoichiometric consequences. If this process is not adequately represented in Earth system models, future terrestrial carbon sink capacity may be systematically overestimated. Explicit representation of phosphorus cycling and its coupling with carbon and nitrogen cycles will therefore be essential for improving projections of the global carbon cycle.

Methods

5.1. GPP data sets used to estimate the vegetation CO_2 sensitivity coefficient

To quantify vegetation productivity responses to rising atmospheric CO_2, we used three long-term gross primary production (GPP) data sets: NIRvGPP, rEC-LUEGPP, and VODCA2GPP. NIRvGPP was the primary

data set; rEC-LUEGPP and VODCA2GPP were used to test robustness.

NIRvGPP is derived from an empirical relationship between GPP and the near-infrared reflectance of vegetation (NIRv), which combines total near-infrared reflectance and the normalized difference vegetation index (NDVI) and has been widely used to characterize vegetation photosynthetic activity [60]. It is based on long-term AVHRR satellite observations and does not require auxiliary environmental drivers [25]; it has monthly resolution, an original spatial resolution of 0.5° × 0.5°, and covers 1982–2018.

rEC-LUEGPP is generated with a revised light-use efficiency (LUE) model that incorporates CFE through a scaling factor representing the direct effect of CO_2 on LUE [60]; 8-day resolution, 0.05° × 0.05°, 1982–2017.

VODCA2GPP is constructed from the vegetation optical depth (VOD) climate archive and explicitly incorporates CFE [61]; being mainly microwave-based, it is less affected by cloud contamination; monthly resolution, 0.25° × 0.25°, 1988–2020.

All data sets were harmonized to 1° × 1° and analyses restricted to 1982–2015. Unless otherwise noted, analyses used the growing season only, defined per grid cell as months with mean air temperature above 0°C; where temperature remained above 0°C year-round, all months were included.

5.2. Climate and environmental drivers

Monthly air temperature (TMP), precipitation (PRE), and VPD were obtained from CRU TS v4.08 (0.5° × 0.5°); VPD was calculated from monthly 2-m air temperature and dew point temperature. Surface solar shortwave radiation (SSRD), soil moisture (SM; surface-layer soil water, SWVL1), and LAI were obtained from ERA5. Atmospheric CO_2 was the monthly Mauna Loa record. Nitrogen and phosphorus deposition data (1980–2013) were obtained from the global gridded atmospheric deposition products of Wang et al. (2017), available at Figshare (https://figshare.com/s/898e5d6c4f0982674ae3). Stoichiometric ratios for soils, vegetation, and litter were obtained from CABLE model outputs. All variables were restricted to 1982–2015 and resampled to 1° × 1°.

5.3. Identification of land-use change and classification of vegetation types

To reduce the influence of land-use change and management, we used LUH2 v2h to exclude grid cells that (1) experienced a shift in dominant vegetation functional type during the study period, or (2) where the fractional coverage of the dominant land-use type changed by more than 20%. Cropland cells were also excluded because irrigation, fertilization, and cultivation obscure natural-ecosystem responses to elevated CO_2. Vegetation functional types were classified using MODIS MCD12C1 (Collection 6.1; 0.05° × 0.05°), aggregated to 1° × 1° by the dominant-area method.

5.4. Identification of regions of intensifying phosphorus limitation

We conducted paired simulations under identical climate forcing using the carbon–nitrogen–phosphorus (CNP) and carbon–nitrogen (CN) configurations of CABLE, and defined a phosphorus limitation intensity index (PLI):

$PLI = NPP_{CN} - NPP_{CNP}$ (1)

Here, NPP_CN is net primary productivity (NPP) simulated without explicit phosphorus limitation and NPP_CNP is NPP simulated with explicit phosphorus limitation. Because the CNP configuration imposes phosphorus constraints that CN does not, NPP_CNP ≤ NPP_CN, so PLI ≥ 0 and represents the NPP suppressed by phosphorus limitation under identical climate forcing [18]. Larger PLI values indicate stronger phosphorus limitation. Conceptually, this is analogous to the net productivity response derived from phosphorus-addition experiments [53], and provides a feasible means of quantifying phosphorus limitation continuously at the global scale [47].

We analyzed the temporal trend in PLI for each grid cell over 1982–2015 (linear-regression slope; significance by the Mann–Kendall test). A significantly positive PLI trend indicates intensifying phosphorus limitation. We defined regions of intensifying phosphorus limitation as grid cells with positive IPL trends whose slopes fell within the upper 80% of the slope distribution and were significant at $p < 0.01$. Regions not included are not necessarily free of phosphorus limitation; they may have experienced weaker intensification or no significant increase. Under this threshold, such regions concentrate in the temperate mid- to high-latitudes of the Northern Hemisphere and in tropical savanna zones, including parts of central North America, Europe and northern Eurasia, the Sahel, tropical South American grassland regions, and northeastern Australia.

Sensitivity tests using the 40th and 60th percentiles as alternative thresholds confirmed that the main conclusions were robust (Figs. S9, S10). As IPL is derived from a single land-surface model (CABLE), the spatial delineation of intensifying-limitation regions is model-dependent; however, all productivity diagnostics within these regions rely on independent satellite and reanalysis data (Sections 2.1–2.2), mitigating circularity.

5.5. Estimation of the vegetation CO_2 sensitivity coefficient

We estimated the vegetation CO_2 sensitivity coefficient using a multivariate linear regression with environmental covariates and interaction terms:

$$y = \beta \cdot \mathrm{CO_2} + \mathrm{C_1} \cdot \mathrm{VPD} + \mathrm{C_2} \cdot \mathrm{T} + \mathrm{C_3} \cdot (\mathrm{CO_2} \cdot \mathrm{VPD}) + \mathrm{C_4} \cdot (\mathrm{CO_2} \cdot \mathrm{T}) + \mathrm{C_5} + \epsilon$$

2

Here, y is the growing-season GPP time series; CO_2, VPD, and T are atmospheric CO_2, vapor pressure deficit, and air temperature; β is the regression coefficient on the CO_2 term (i.e., the vegetation CO_2 sensitivity coefficient); C_1–C_4 are the coefficients of the covariates and their interactions with CO_2; C_5 is the intercept; and ε is the residual term. All variables were expressed as anomalies (annual value minus

the mean within the corresponding 15-year moving window). β was estimated per grid cell by ordinary least squares within a 15-year moving window over 1982–2015, and standardized as the percentage change in GPP per 100-ppm increase in atmospheric CO_2 (% per 100 ppm) [3].

Note that VPD and temperature enter Eq. (2) as covariates to isolate the CO_2-driven component of GPP from concurrent hydrothermal variability; this differs from their role in the structural equation model (Section 2.7), where they are treated as independent drivers. β therefore quantifies CO_2 sensitivity after accounting for VPD and temperature and is not confounded by them.

5.6. Interannual GPP increments and trend analysis

We calculated the interannual increment in GPP (ΔGPP), defined as the change between consecutive years:

$$\Delta GPP(t) = GPP(t) - GPP(t-1) \quad (3)$$

A long-term decline in ΔGPP indicates a slowdown in the rate of productivity gain. For β, ΔGPP, LAI, and hydroclimatic variables (TMP, SM, VPD), temporal changes were characterized by trend slopes and significance assessed with the Mann–Kendall test [62]. Unless otherwise stated, $p \leq 0.05$ was considered significant.

5.7. Covariance-based structural equation modeling

We used covariance-based SEM (CB-SEM) to compare driver effects on GPP globally and within regions of intensifying phosphorus limitation [63]. Variables were CO_2, VPD, TMP, PRE, LAI, leaf N:P, and GPP; nitrogen and phosphorus deposition were additionally included to assess their influence on leaf N:P. Separate models were fitted for the global domain and for regions of intensifying phosphorus limitation. All variables were standardized; parameters were estimated with 1,000 bootstrap resamples. Model performance was evaluated with CFI, TLI, and RMSEA.

Declarations

Conflict of Interest

The authors declare no conflicts of interest relevant to this study.

Data Availability Statement

All input datasets used in this study are publicly available. The NIRvGPP dataset (Wang et al., 2021) can be accessed at https://doi.org/10.6084/m9.figshare.12981977.v2, and the rEC-LUE GPP dataset (Zheng et al., 2020) is available at https://doi.org/10.6084/m9.figshare.8942336.v1. The VODCA2 GPP product (Wild et al., 2022) is archived at https://doi.org/10.5281/zenodo.5553516, with the accompanying paper available at https://doi.org/10.5194/essd-14-1063-2022. The CRU TS4.08 climate dataset (Harris et al., 2020), from which temperature (TMP) and precipitation (PRE) were directly obtained and vapor pressure

deficit (VPD) was calculated from temperature and vapor pressure, is accessible at https://crudata.uea.ac.uk/cru/data/hrg/. ERA5 monthly reanalysis data (Hersbach et al., 2020), including surface solar radiation downwards (SSRD) and volumetric soil water layer 1 (SWVL1), are provided by the Copernicus Climate Change Service (C3S) at https://doi.org/10.24381/cds.f17050d7. Atmospheric CO_2 concentration data from the Mauna Loa Observatory were provided by NOAA/GML (Dr. Pieter Tans) and Scripps Institution of Oceanography (Dr. Ralph Keeling), available at https://gml.noaa.gov/ccgg/trends/. The Land-Use Harmonization dataset (LUH2 v2h; Hurtt et al., 2020) can be downloaded from http://luh.umd.edu/data.shtml, and the MODIS Land Cover product (MCD12C1, version 6.1; Friedl & Sulla-Menashe, 2022) is available through the NASA LP DAAC platform at https://doi.org/10.5067/MODIS/MCD12C1.061. Source data supporting this study are available in Zenodo (Zhang et al., 2026), at https://doi.org/10.5281/zenodo.21272532.

Code availability

All analyses were conducted in Python (version 3.10.11). The algorithms are fully described in the Methods section. No custom code was developed beyond the standard implementation of these equations.

Author Contributions

Conceptualization: Jing Peng, Zhuo Zhang.

Methodology: Zhuo Zhang, Chengjin Chu, Wenjie Dong.

Software: Zhuo Zhang,Li Dan, Yaping Chen.

Validation: Zhuo Zhang, Jing Peng.

Formal analysis: Zhuo Zhang, Jing Peng.

Resources: Jing Peng, Li Dan,Yaping Chen.

Data Curation: Zhuo Zhang, Wenjie Dong.

Writing - Original Draft: Zhuo Zhang.

Writing - Review & Editing: Jing Peng, Zhuo Zhang, Chengjin Chu, Wenjie Dong, Li Dan, Yaping Chen.

Visualization: Zhuo Zhang, Yaping Chen.

Supervision: Jing Peng.

Project Administration: Jing Peng.

Funding Acquisition: Jing Peng.

Acknowledgments

This study is supported by the National Key Research and Development Program of China (2023YFF0805501), National Natural Science Foundation of China (NSFC) project (42575136), Shenzhen Science and Technology Program (JCYJ20250604174743057) and Guangdong Provincial Field Observation and Research Station for Biodiversity and Biotic Interactions in Chebaling Lingnan Mountain Forests (2025B1212050003). We thank for the technical support of the National Large Scientific and Technological Infrastructure“Earth System Numerical Simulation Facility”(https://cstr.cn/31134.02.EL).

References

1. Friedlingstein, P. et al. Global carbon budget 2024. *Earth System Science Data*. **17(3)**, 965–1039 (2025).
2. Ruehr, S. et al. Evidence and attribution of the enhanced land carbon sink. *Nature Reviews Earth & Environment*. **4**, 518–534 (2023).
3. Wang, S. et al. Recent global decline of CO2 fertilization effects on vegetation photosynthesis. *Science*. **370(6522)**, 1295–1300 (2020).
4. Keenan, T. F. et al. Increase in forest water-use efficiency as atmospheric carbon dioxide concentrations rise. *Nature*. **499(7458)**, 324–327 (2013).
5. Guerrieri, R. et al. Disentangling the role of photosynthesis and stomatal conductance on rising forest water-use efficiency. *Proceedings of the National Academy of Sciences*. **116(34)**, 16909–16914(2019).
6. Liu, Y. et al. Field-experiment constraints on the enhancement of the terrestrial carbon sink by CO2 fertilization. *Nature Geoscience*. **12(10)**, 809–814 (2019).
7. Keenan, T. F. et al. A constraint on historic growth in global photosynthesis due to rising CO2. *Nature Climate Change*. **13(12)**, 1376–1381(2023).
8. Piao, S., Yue, C., Ding, J., & Guo, Z. Perspectives on the role of terrestrial ecosystems in the ‘carbon neutrality’ strategy. *Science China Earth Sciences*.***65(6)***, 1178–1186(2022).
9. Du, E., de Vries, W., Collalti, A., & De Marco, A. Climate warming alters nutrient cycling and its constraint on CO2 fertilization in global forests. *Current Climate Change Reports*. **11**, 3 (2025).
10. Lin, S. et al. Global vegetation production may decrease in this century due to rising atmospheric dryness. *Nature Ecology & Evolution*. **9(12)**, 2279–2289(2025).
11. Li, S. et al. Vegetation growth due to CO2 fertilization is threatened by increasing vapor pressure deficit. *Journal of Hydrology*. **619**, 129292 (2023).
12. Adams, M. A., Buckley, T. N., & Turnbull, T. L. Diminishing CO2-driven gains in water-use efficiency of global forests. *Nature Climate Change*. **10**, 466–471 (2020).
13. Li, F. et al. Dryland dominance in the slowdown of global vegetation carbon uptake. *Nature Geoscience*. **19**, 542–548(2026).

14. Vallicrosa, H., Sardans, J., Maspons, J., & Peñuelas, J. Global distribution and drivers of forest biome foliar nitrogen to phosphorus ratios (N:P). *Global Ecology and Biogeography*. **31**, 861–871 (2022).
15. Wright, I. J. et al. Global climatic drivers of leaf size. *Science*.**357(6354)**, 917–921 (2017).
16. Peng, Z. et al. Foliar nutrient resorption stoichiometry and microbial phosphatase catalytic efficiency together alleviate the relative phosphorus limitation in forest ecosystems. *New Phytologist*. **238(3),** 1033–1044 (2023).
17. Reich, P. B., Hobbie, S. E., & Lee, T. D. Plant growth enhancement by elevated CO2 eliminated by joint water and nitrogen limitation. *Nature Geoscience*. **7**, 920–924(2014).
18. Terrer, C. et al. Nitrogen and phosphorus constrain the CO2 fertilization of global plant biomass. *Nature Climate Change*. **9**, 684–689 (2019).
19. Smith, W. K. et al. Large divergence of satellite and Earth system model estimates of global terrestrial CO2 fertilization. *Nature Climate Change*.**6**, 306–310 (2016).
20. Wang, Z. et al. Compartmentalized homeostasis drives high bamboo forest productivity under nutrient imbalance. *Advanced Science*. **13(11)**, e17442 (2025).
21. Wang, S. et al. Phosphorus constrains global photosynthesis more than nitrogen does. *Nature Ecology & Evolution*. **9**, 2025–2035(2025).
22. Jiao, W., Wang, L., Smith, W. K., Chang, Q., Wang, H., & D'Odorico, P. Observed increasing water constraint on vegetation growth over the last three decades. *Nature Communications*. **12**, 3777(2021).
23. Li, C. et al. Long-term leaf nitrogen and phosphorus dynamics and drivers in China's forests under global change. *Forest Ecosystems*. **13**, 100325 (2025).
24. Keane, J. B. et al. Grassland responses to elevated CO2 determined by plant–microbe competition for phosphorus. *Nature Geoscience*. **16**, 704–709 (2023).
25. Jiang, M. et al. Low phosphorus supply constrains plant responses to elevated CO2: A meta-analysis. *Global Change Biology*. **26,** 5856–5873(2020).
26. Luo, X. et al. Long-term atmospheric nitrogen deposition enhances forest production by suppressing microbial competition for phosphorus. *Global Change Biology*. **31(6)**, e70264 (2025).
27. Yu, Q. et al. Decadal nutrient addition reveals phosphorus limitation and its adaptive mechanisms in tropical rainforests. *Soil Biology and Biochemistry*. **211**, 109976 (2025).
28. Hou, E. et al. Global meta-analysis shows pervasive phosphorus limitation of aboveground plant production in natural terrestrial ecosystems. *Nature Communications*. **11**, 637 (2020).
29. Li, C. et al. Silicate chemical weathering disrupts the global patterns of phosphorus limitation. *Nature Communications*. **16,** 10742 (2025).
30. Luo, M., Moorhead, D. L., Ochoa-Hueso, R., Mueller, C. W., Ying, S. C., & Chen, J. Nitrogen loading enhances phosphorus limitation in terrestrial ecosystems with implications for soil carbon cycling. *Functional Ecology*. **36(11)**, 2845–2858(2022).

31. Thingstad, T. F. et al. Nature of phosphorus limitation in the ultraoligotrophic eastern Mediterranean. *Science*.**309(5737)**, 1068–1071(2005).
32. Elser, J. J., Fagan, W. F., Kerkhoff, A. J., Swenson, N. G., & Enquist, B. J. Biological stoichiometry of plant production: Metabolism, scaling and ecological response to global change. *New Phytologist*. **186(3)**, 593–608 (2010).
33. Kong, X., Wang, B., Bian, S., Chen, Y., Li, M., & Fan, W. Spatial and temporal trends in the response of global forest GPP and NEP to CO2 fertilization effects from 1982 to 2015. *National Remote Sensing Bulletin*. **29(1)**, 102–117(2025).
34. Yang, N. et al. Leaf economic strategies drive global variation in phosphorus stimulation of terrestrial plant production. *Nature Communications*. **16**, 5562(2025).
35. Yu, G., & Yan, J. From rhizosphere to resorption: Comparing phosphorus adaptation in trees and herbs under decadal acid rain stress. *Bulletin of the Ecological Society of America*. **106(3)**, e70015(2025).
36. Descals, A., Janssens, I. A., & Peñuelas, J. Amazon forest nutrient limitation is mitigated by distant fire emissions. *Nature Geoscience*. **19**, 291–295(2026).
37. Wei, N., & Xia, J. Robust projections of increasing land carbon storage in boreal and temperate forests under future climate change scenarios. *One Earth* . **7(1)**, 88–99 (2024).
38. Walker, A. P. et al. Integrating the evidence for a terrestrial carbon sink caused by increasing atmospheric CO2. *New Phytologist*. **229(5)**, 2413–2445 (2021).
39. Lian, X., Jiao, L., & Liu, Z. Saturation response of enhanced vegetation productivity attributes to intricate interactions. *Global Change Biology*. **29**, 1080–1095 (2023).
40. Li, F. et al. Global water use efficiency saturation due to increased vapor pressure deficit. *Science*. **381(6658)**, 672–677 (2023).
41. Huang, J. et al. Mycorrhizal symbiosis alleviates nitrogen-induced phosphorus limitation in terrestrial ecosystems. *Global Biogeochemical Cycles*. **40**, e2025GB008775 (2026).
42. Dong, T. et al. Deciphering the variability of leaf phosphorus-allocation strategies using leaf economic traits and reflectance spectroscopy across diverse forest types. *New Phytologist.***247(3)**, 1129–1144(2025).
43. Ibrahim, M. M. et al. A critical review of carbon and phosphorus linkages in soils. *Global Change Biology*. **32(3)**, e70804(2026).
44. Cotrufo, M. F. et al. Formation of soil organic matter via biochemical and physical pathways of litter mass loss. *Nature Geoscience*.**8**, 776–779 (2015).
45. Peñuelas, J., Zheng, B., Tariq, A., & Sardans, J. Microbial phosphorus cycling in terrestrial ecosystems. *Nature Reviews Microbiology*. (2026)
46. Wang, Y. P., Law, R. M., & Pak, B. A global model of carbon, nitrogen and phosphorus cycles for the terrestrial biosphere. *Biogeosciences*.**7**, 2261–2282 (2010).

47. Peng, J., Dan, L., & Tang, X. Phosphorus limitation on carbon sequestration in China under RCP8.5. *Advances in Atmospheric Sciences*. **40**, 1187–1198 (2023).
48. Fan, Y. et al. Variation in leaf phosphorus fractions reflects plant adaptations and distribution in low-phosphorus tropical forests. *Functional Ecology***39**, 621–634 (2025).
49. Shen, H. et al. Postfire phosphorus enrichment mitigates nitrogen loss in boreal forests. *Environmental Science & Technology*. **58(24)**, 10611–10622 (2024).
50. Ding, W., Cong, W. F., & Lambers, H. Plant phosphorus-acquisition and -use strategies affect soil carbon cycling. *Trends in Ecology & Evolution*. **36**, 899–906 (2021)
51. Wang, X. et al. Long-term nitrogen deposition inhibits soil priming effects by enhancing phosphorus limitation in a subtropical forest. *Global Change Biology*. **29(14)**, 4081–4093(2023)
52. Ellsworth, D. S. et al. Convergence in phosphorus constraints to photosynthesis in forests around the world. *Nature Communications*. **13**, 5005(2022).
53. Cunha, H. F. V. et al. Direct evidence for phosphorus limitation on Amazon forest productivity. *Nature*. **608**, 558–562(2022).
54. Jiang, M. et al. Microbial competition for phosphorus limits the CO2 response of a mature forest. *Nature*. **630**, 660–665 (2024).
55. Li, F. et al. Effects of elevated carbon dioxide on plant growth and leaf photosynthesis of annual ryegrass along a phosphorus deficiency gradient. *Frontiers in Plant Science*. **14**, 1271262 (2023).
56. Wang, Z. et al. Phosphorus limitation on CO2 fertilization effect in tropical forests informed by a coupled biogeochemical model. *Forest Ecosystems*. **11**, 100210 (2024).
57. Wieder, W. R., Cleveland, C. C., Smith, W. K., & Todd-Brown, K. Future productivity and carbon storage limited by terrestrial nutrient availability. *Nature Geoscience*. **8**, 441–444(2015).
58. Chen, Z. et al. Global phosphorus enrichment reshapes terrestrial phosphorus cycling. *Global Change Biology*. **32(4)**, e70827(2026).
59. Wang, S., Zhang, Y., Ju, W., Qiu, B., & Zhang, Z. Tracking the seasonal and inter-annual variations of global gross primary production during last four decades using satellite near-infrared reflectance data. *Science of the Total Environment*. **755**, 142569(2021).
60. Zheng, Y. et al. Improved estimate of global gross primary production for reproducing its long-term variation, 1982–2017. *Earth System Science Data*. **12**, 2725–2746 (2020).
61. Wild, B. et al. VODCA2GPP – a new, global, long-term (1988–2020) gross primary production dataset from microwave remote sensing. *Earth System Science Data*.**14(3)**, 1063–1085(2022).
62. Liu, Z. et al. Increased early-season productivity drives earlier peak of vegetation photosynthesis across the Northern Hemisphere. *Commun Earth Environ***6**, 157 (2025).
63. Zhong, Z., Chen, H. W., He, B., & Su, B. Contrasting vegetation productivity responses in arid and humid zones to recent changes in diurnal temperature range. *The Innovation Geoscience*. **3(4)**, 100163(2025).

Figures

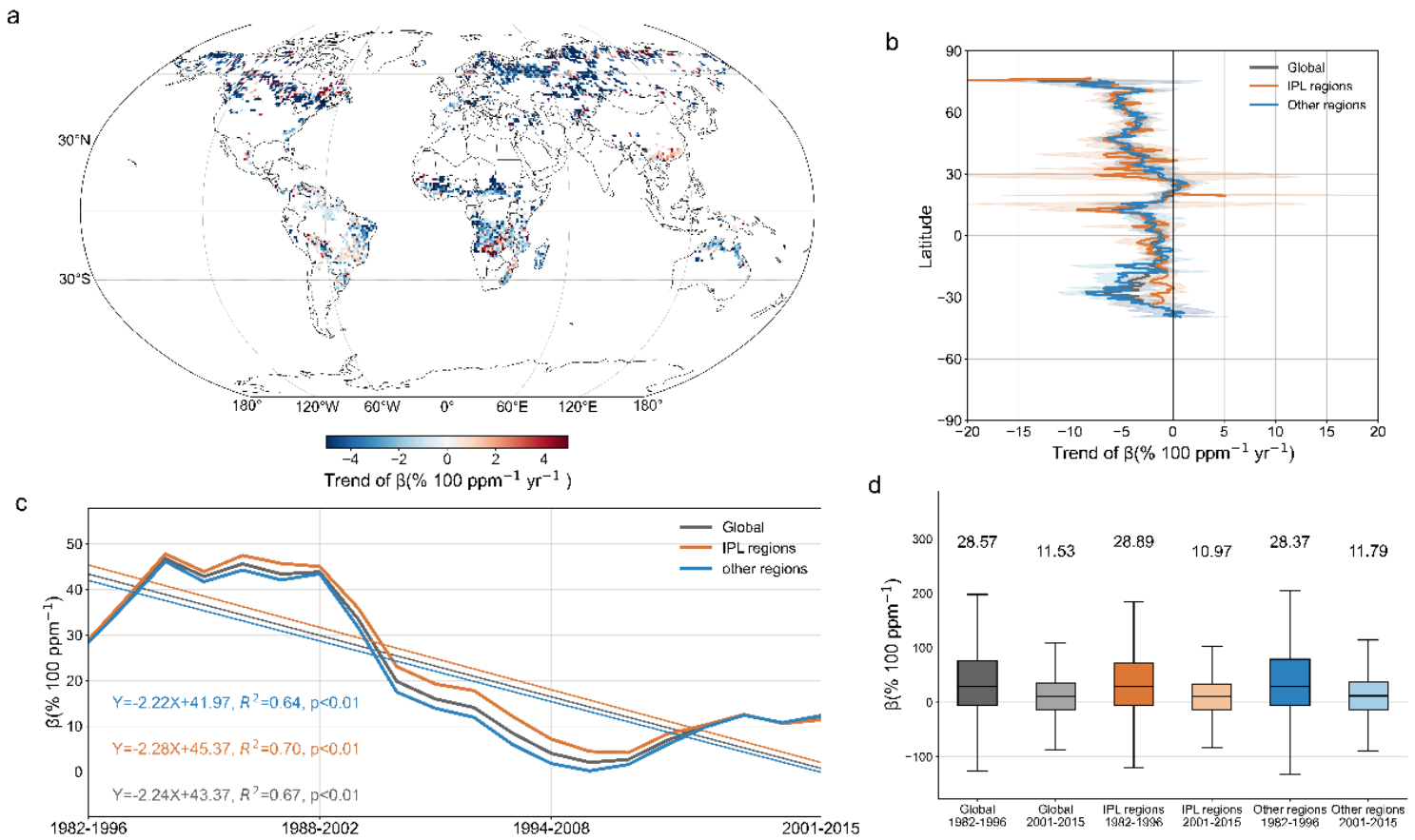

Figure 1

Accelerated decline of β in regions experiencing intensifying phosphorus limitation, 1982–2015. (a) Spatial pattern of β trends across intensifying phosphorus-limitation (IPL) regions. (b) Latitudinal profiles of β trends for the globe, IPL regions, and regions without intensifying phosphorus limitation (other regions); shaded bands denote the 95% confidence intervals. (c) Temporal time-series of β for the globe, IPL regions, and other regions. (d) Box-plot comparisons of β between two sub-periods across the globe and IPL regions. Boxes show the interquartile range (IQR), solid horizontal lines mark median values, and median β values for each period are annotated above each box.

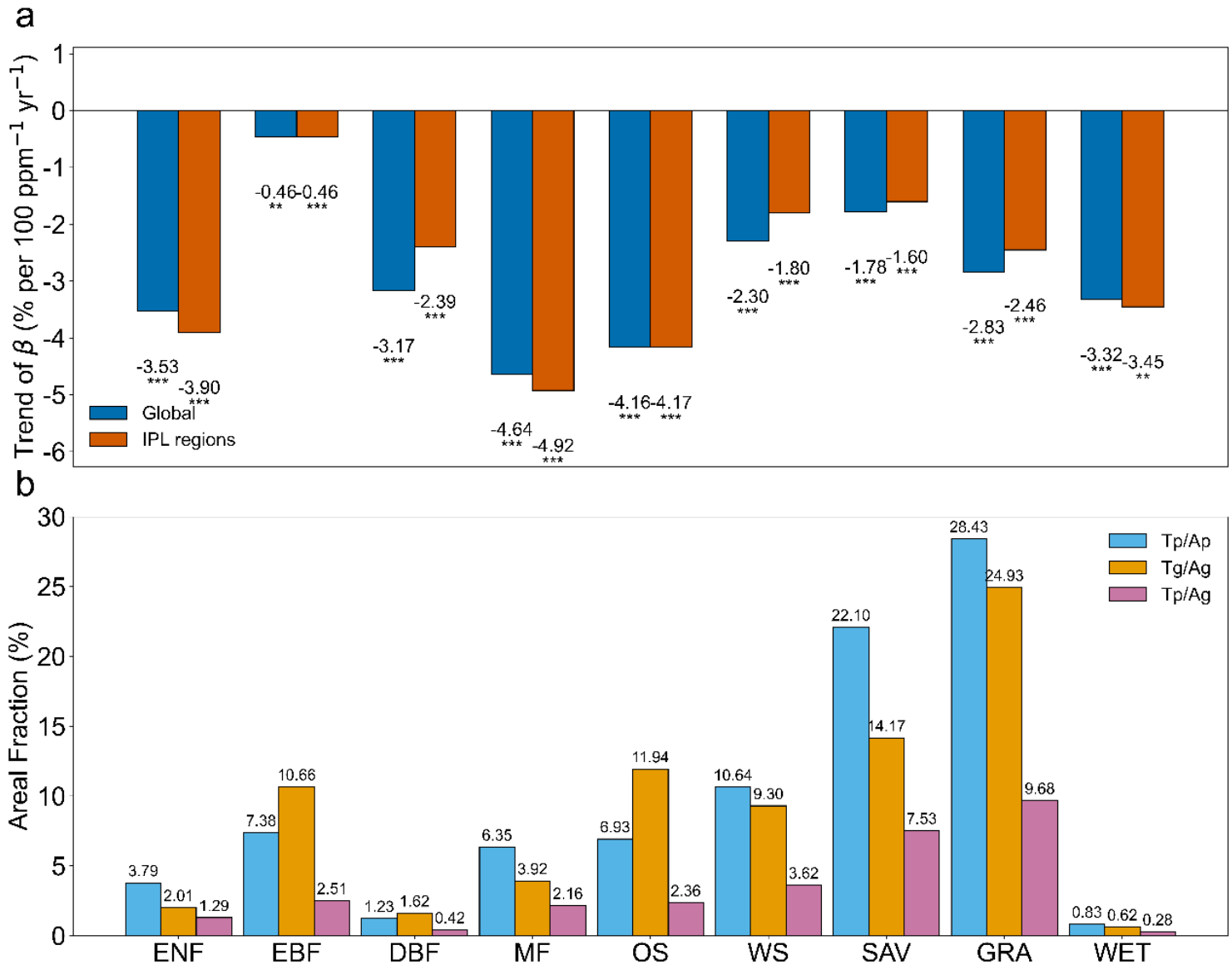

Figure 2

Declining trends of β and land area proportions across different vegetation types at both global and IPL regions. Area proportions include: Tp/Ap (proportion of the specific vegetation type relative to the total area of IPL regions), Tg/Ag (proportion relative to the total global land area), and Tp/Ag (proportion of the specific vegetation type within IPL regions relative to the total global land area).

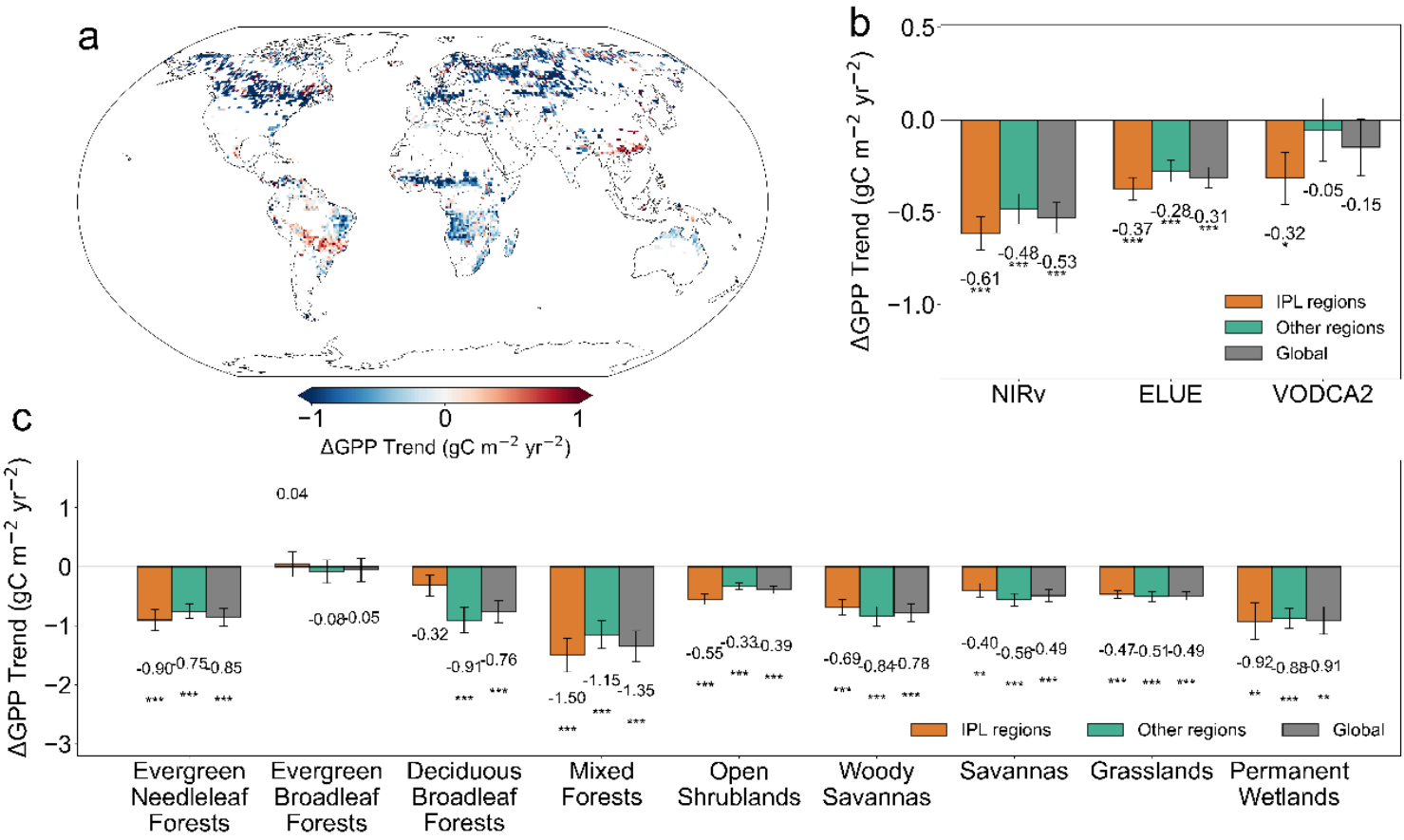

Figure 3

Accelerated decline in the interannual increment of GPP (ΔGPP) in IPL regions. (a) Spatial distribution of ΔGPP trends within IPL regions. (b) Comparison of ΔGPP trends between global and IPL regions derived from multiple GPP datasets. (c) Comparison of ΔGPP trends across different vegetation types at both global and IPL regions.

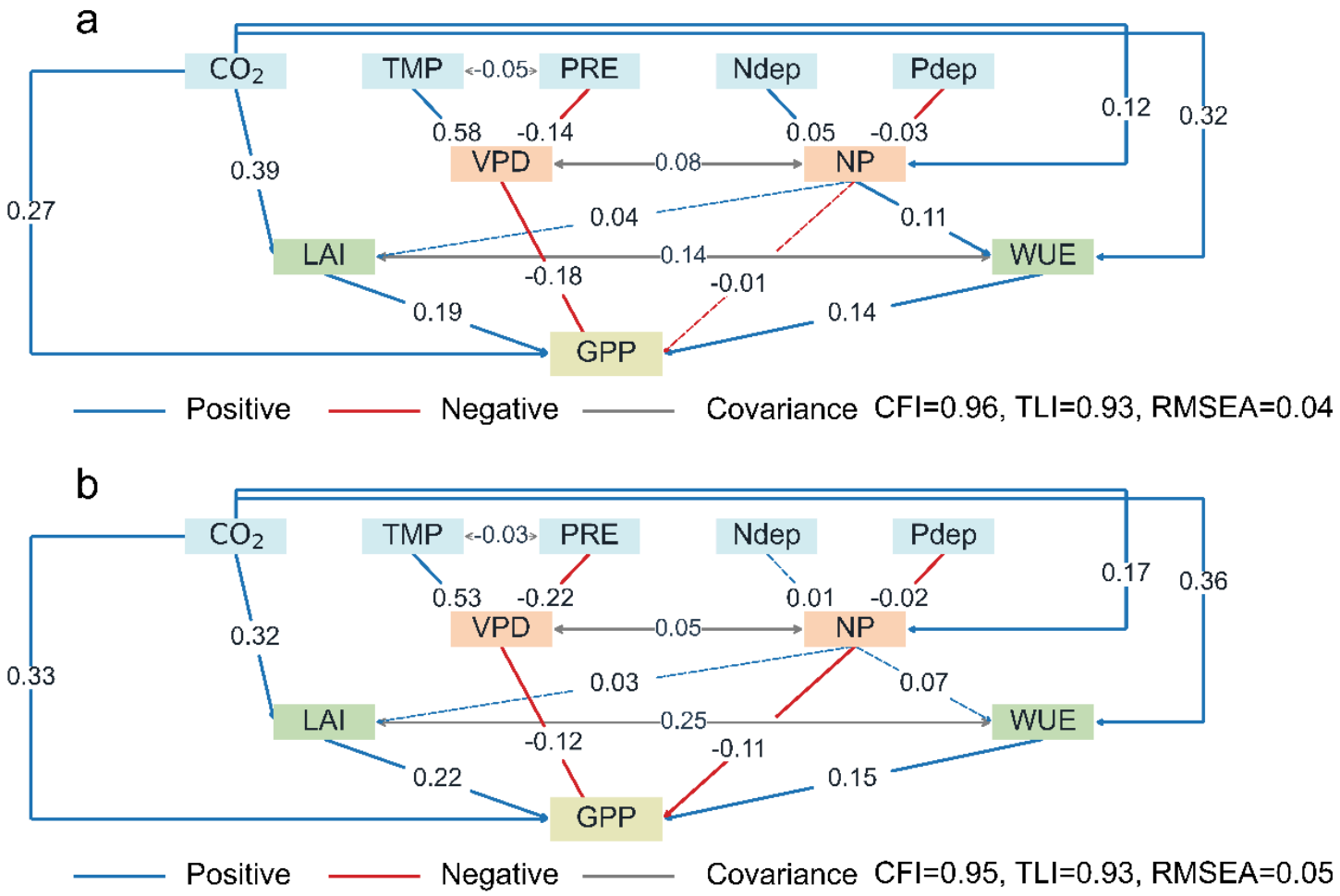

Figure 4

Comparison of Structural Equation Models (SEM) for GPP and climatic factors between global and IPL regions. (a) Global-scale SEM. (b) SEM for IPL regions. Solid lines represent significant effects ($p<0.05$). Model variables include vapor pressure deficit (VPD), temperature (TMP), precipitation (PRE), leaf area index (LAI), leaf N:P ratio (NP), nitrogen deposition (Ndep), phosphorus deposition (Pdep), and atmospheric CO_2 (CO2).

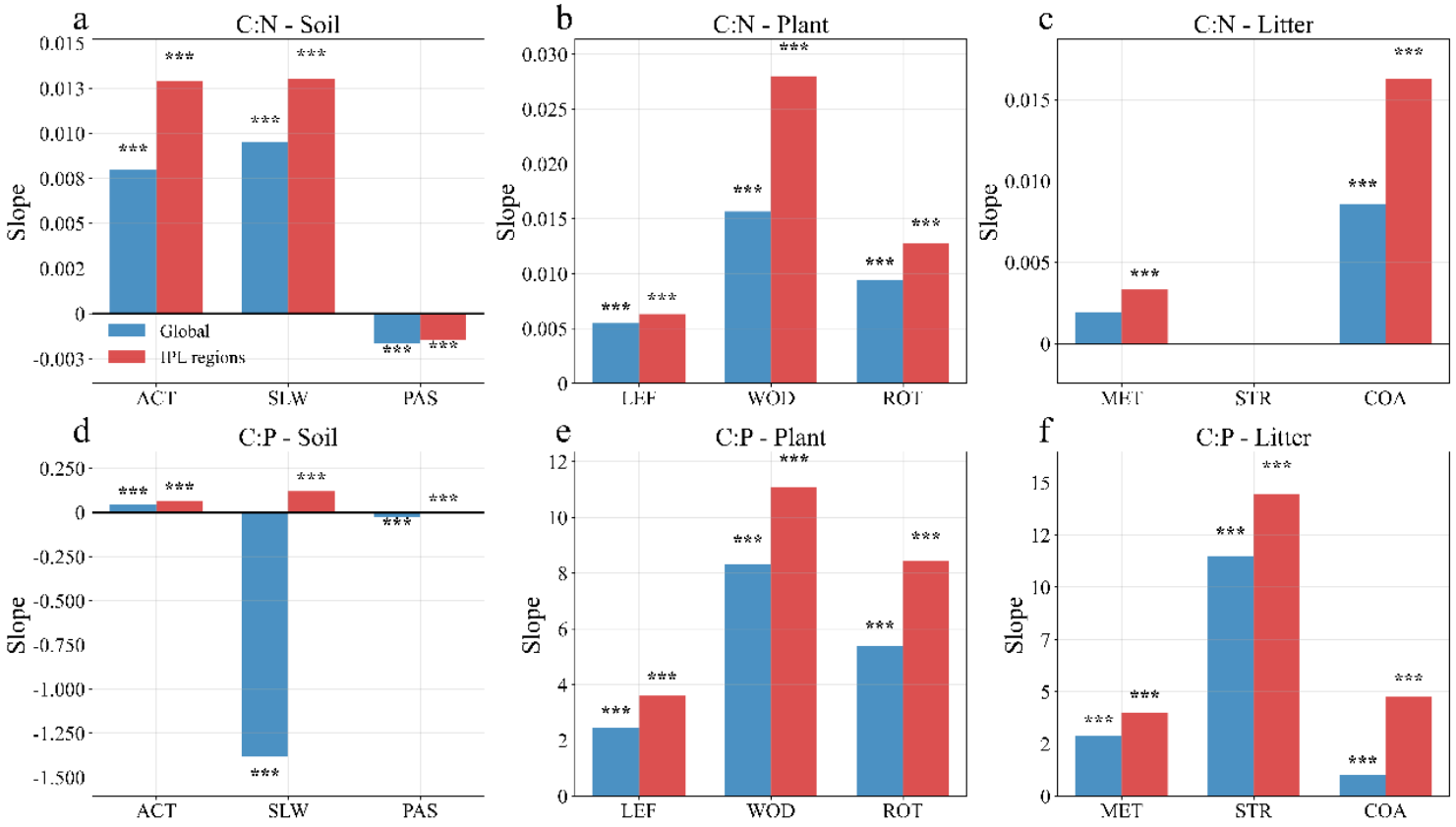

Figure 5

Temporal trends in carbon-to-nitrogen (C:N) and carbon-to-phosphorus (C:P) ratios across soil, plant, and litter pools during 1982–2015. The trends are compared between the globe and IPL regions. The soil pool is categorized into active (ACT), slow (SLW), and passive (PAS) pools; the litter pool is classified by decomposition rate into metabolic (MRT), structural (STR), and coarse/woody (COA) pools; and the plant pool is divided by organ type into leaves (LEF), wood (WOD), and roots (ROT).

Supplementary Files

This is a list of supplementary files associated with this preprint. Click to download.

- SupportingInformation.pdf